

1 **Modeling of the Influence of Sea Ice Cycle and Langmuir Circulation on the**
2 **Upper Ocean Mixed Layer Depth and Freshwater Distribution at the West**
3 **Antarctic Peninsula**

4
5 **C. Schultz¹, S. C. Doney¹, W. G. Zhang², H. Regan³, P. Holland⁴, M. Meredith⁴, S. Stammerjohn⁵**

6
7 ¹ University of Virginia, Department of Environmental Sciences, Charlottesville, VA, USA

8 ² Woods Hole Oceanographic Institution, Woods Hole, MA, USA

9 ³ Univ. Brest, CNRS, IRD, Ifremer, Laboratoire D'Océanographie Physique et Spatiale, IUEM,
10 Brest, France

11 ⁴ British Antarctic Survey, Natural Environment Research Council, Cambridge, UK

12 ⁵ Institute of Arctic and Alpine Research, University of Colorado, Boulder, CO, USA

13
14 Corresponding author: Cristina Schultz (cs3xm@virginia.edu)

- 15
16
17 • Sea-ice redistribution had a large impact on the mixed layer depth seasonality and
18 interannual variability in the West Antarctic Peninsula
19 • In the West Antarctic Peninsula, areas of high summer sea-ice melt can show net annual
20 freezing due to high sea-ice formation in winter
21 • Including a parameterization for Langmuir Circulation based on entrainment below the
22 mixed layer improved the simulated mixed layer depth
- 23
24
25
26
27
28
29
30
31
32
33
34
35
36
37

38

39 **Abstract**

40 The Southern Ocean is chronically under-sampled due to its remoteness, harsh environment
41 and sea-ice cover. Ocean circulation models yield significant insight into key processes and to
42 some extent obviate the dearth of data, however they often underestimate surface mixed layer
43 depth (MLD), with consequences for water-column properties. In this study, a coupled
44 circulation and sea-ice model was implemented for the region adjacent to the West Antarctic
45 Peninsula (WAP), a climatically sensitive region which has exhibited decadal trends toward
46 higher temperatures, a shorter sea-ice season and increasing glacial freshwater input, overlain
47 by strong interannual variability. Hindcast simulations were conducted with different air-ice
48 drag coefficients and Langmuir-circulation parameterizations to determine the impact of these
49 factors on MLD. Including Langmuir circulation deepened the surface mixed layer, with the
50 deepening being more pronounced in the shelf and slope regions. Optimal selection of an air-
51 ice drag coefficient also increased the modeled MLD by similar amounts, and had a larger
52 impact in improving the reliability of the simulated MLD interannual variability. This study
53 highlights the importance of sea ice volume and redistribution to correctly reproduce the
54 physics of the underlying ocean, and the potential of appropriately parameterizing Langmuir
55 circulation to help correct for a bias towards shallow MLD in the Southern Ocean. The model
56 also reproduces observed freshwater patterns in the WAP during late summer and suggests
57 that areas of intense summertime sea-ice melt can still show net annual freezing due to high
58 sea-ice formation during the winter.

59

60

61

62 **1 Introduction**

63 The coastal ocean on the western side of the West Antarctic Peninsula (WAP) has
64 undergone dramatic changes over the past several decades. During the second half of the 20th
65 century, the WAP region showed the highest atmospheric warming in the Southern Hemisphere
66 (Vaughan et al, 2003), a decrease in the duration of the sea-ice season (Stammerjohn et al.,
67 2008) and an accelerating retreat of 80 % of the glaciers in the region (Cook et al, 2005). The
68 surface ocean also exhibited an increase in temperature of more than 1°C (Meredith et al.,
69 2005). The increased surface ocean temperature, thought to be caused by increased
70 temperatures in the atmosphere and the decreased sea-ice cover, could lead to positive
71 feedbacks that would further increase the atmospheric warming. Around the turn of the 21st
72 century, however, the atmospheric warming trend leveled off and even reversed direction in
73 some places (Turner et al., 2016). This trend reversal can be attributed to natural climate
74 variability and indicates that the changes observed in the WAP cannot be explained by large-
75 scale global warming alone.

76 The impact of changes in heat and freshwater input on the vertical ocean mixing have
77 not been fully quantified. While sea-ice melt decreases density of the surface layer and
78 contributes to stronger near-surface stratification, decreased sea-ice cover also leads to
79 increased wind-induced ocean mixing. The effect of sea-ice changes on the surface mixed layer
80 depth (MLD), therefore, relies on a balance between these two competing effects, which is
81 further complicated by laterally redistributing and mechanically thickening sea ice cover. This
82 can also redistribute sea ice melt waters away from where sea ice was formed in situ, thus
83 leading to areas of net sea ice production versus sea ice melt (Meredith et.al., 2008; 2010;
84 2017).

85 Studying the impact of each of these changes on the MLD is important given it may
86 affect not only trends in the distribution of water masses in the region, but also on oceanic
87 primary production, ecosystem dynamics and carbon cycle in the WAP (Vernet et. al., 2008;
88 Legge et. al., 2017). Understanding the impact of increased glacial melt is also important given
89 salinity gradients are thought to contribute to the coastal circulation in the WAP (Moffat et al.,
90 2008), and glacial freshwater can be a major source of dissolved iron for primary production
91 (Annett et al., 2017).

92 One of the challenges of studying the MLD in the WAP is the scarcity of data. Although
93 the Palmer- Long Term Ecological Research (LTER) project has been conducting yearly cruises
94 during January and February since 1993, thus providing an invaluable dataset of over two
95 decades of duration, each cruise constitutes a snapshot relevant to the period of its occupation
96 (Ducklow et al., 2013). Sustained time series with high-frequency sampling exist, including the
97 Rothera Time Series (REF) and stations occupied quasi-weekly adjacent to Palmer Station
98 (Figure 1), however these point measurements at near-coastal sites do not have full spatial
99 extent across the WAP shelf.

100 Innovative technologies such as underwater gliders are helping to obviate this issue
101 (REF); there is great scope in addition for high-resolution regional modeling to aid
102 understanding of key processes and the causes of change. Such models can also be used to
103 diagnose the source and amount of freshwater injected into different areas of the WAP shelf,
104 and to study the influence of different processes (e.g., wind mixing and freshwater-induced
105 stratification) on MLD and other key ocean properties.

106 Surface MLD resolved by ocean models are often too shallow, especially in the Southern
107 Ocean (Noh and Lee, 2008; Belcher et al., 2012; Schiller and Ridgway, 2013), and this bias has
108 been attributed partially to the neglect of Langmuir circulation that results from the interaction
109 between winds and surface waves (Belcher et al., 2012; D'Asaro, 2014). Langmuir circulation
110 (LC) comprises a series of shallow vortices that counter-rotate on a vertical plane in the surface
111 mixed layer. Strong velocity and vertical shear of the velocity in the Langmuir vortices enhance
112 near-surface turbulence, erode stratification at the top of the thermocline, and thus deepen the
113 surface mixed layer (e.g., Li et al., 2013).

114 How wind, waves and Langmuir-induced turbulence might affect MLD and mixing
115 processes in the presence of an ice cover is an active area of research. Although the presence of
116 a consolidated ice cover can greatly attenuate waves, a less consolidated ice cover, which
117 typically characterizes WAP seasonal sea ice, can permit ocean waves to travel 100's of
118 kilometers into the ice cover (e.g., Kohout et al., 2014; 2020/in review), potentially affecting sea
119 ice growth processes (Doble et al., 2003), sea ice distributions (Kohout et al., 2014), sea ice melt
120 and near-surface mixing processes (Smith et al., 2018). Other processes, such as air-sea flux and
121 coastal freshwater input, could also affect the surface MLD.

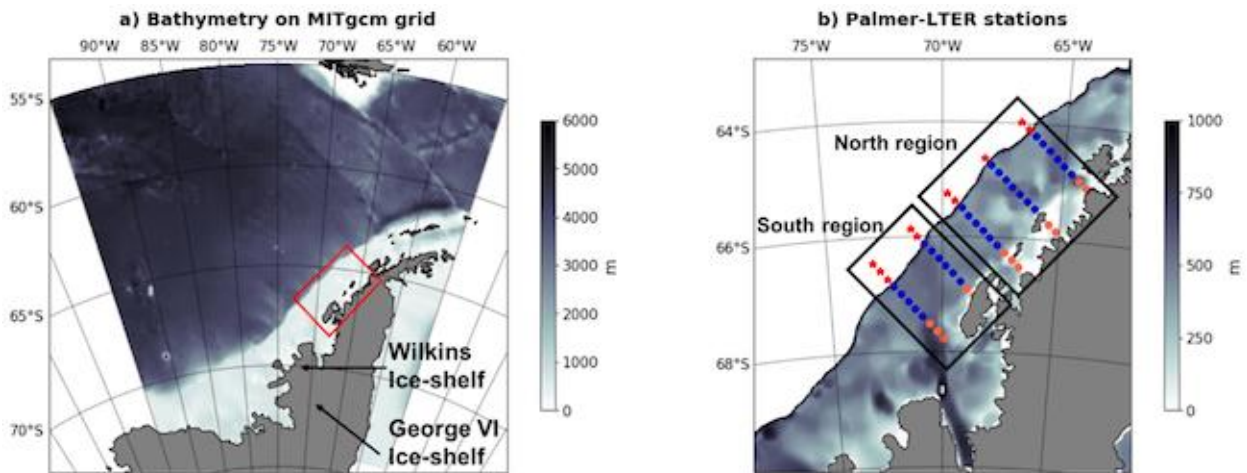
122 As the first part of the Palmer-LTER modeling component to study biophysical and
123 biogeochemical processes on the WAP shelf region, this study aims to understand how different
124 physical factors affect surface MLD in the region, with a view to enabling subsequent works on
125 biophysical and biogeochemical processes on the WAP shelf. To test the influence of LC on the
126 MLD in the WAP region, this study tests two different parameterizations of LC, based on Li et al.
127 (2017) and Li and Fox-Kemper (2017). While these parameterizations have been tested in global
128 models, this is the first study to implement them in a regional Southern Ocean model.
129 Simulations with different wind-ice drag coefficients are also analyzed to evaluate the influence
130 of sea ice and wind mixing on the MLD at both seasonal and interannual time scales. The
131 simulations are also compared to the available freshwater data (based on oxygen isotope
132 analysis of surface seawater samples collected annually) to determine the relative impact of
133 sea-ice production/meltwater and meteoric (glacial and precipitation) freshwater inputs in
134 different areas of the WAP shelf (e.g., Meredith et al., 2017). Results highlight the critical need
135 to correctly incorporate sea ice dynamics in order to properly simulate the ocean physics in the
136 WAP.

137 138 **2 Methods**

139 140 2.1 Model and Grid Description

141
142 This study uses a hydrostatic version of the Massachusetts Institute of Technology General
143 Circulation Model (MITgcm) and the embedded sea-ice and ice shelf modules. MITgcm solves
144 Boussinesq Navier-Stokes equations with the hydrostatic assumption on Arakawa-C grid and z-
145 level (fixed depth) vertical layers (Marshall et al., 1997a; 1997b). The sea-ice component of the
146 model is based on Hibler-type ice thermodynamics and elastic-viscous-plastic (EVP) ice
147 rheology (Losch et al. 2010). The ice-shelf component (Losch, 2008) is also used here to include
148 the freshwater input from ice shelf melt. MITgcm has been successfully used to resolve large-
149 scale circulation, sea-ice dynamics and biogeochemistry of the Southern Ocean with horizontal
150 resolutions on the order of a degree of latitude and longitude (Holland et al., 2014; Hauck et al.,
151 2015; Taylor et al., 2013).

152 The model used in this study is a development of that presented in Regan et al. (2018).
 153 It covers a region ranging from 74.7°S, 95°W in the southwest to 55°S, -55.6°W in the northeast
 154 and includes the Bellingshausen Sea, the full extent of the WAP and the Drake Passage (Figure
 155 1a). The model domain was chosen to extend from the southern Bellingshausen Sea (and
 156 includes also the southern ice shelves, the Wilkins and George VI ice shelves), to north across
 157 the Drake Passage to the southern tip of Chile. It therefore includes the Antarctic Circumpolar
 158 Current (ACC) that traverses this domain, flowing northeastward along the shelf break and
 159 affecting shelf break processes. The grid is curvilinear with 0.2 degrees of resolution for latitude
 160 and resolution varying between 0.0538 and 0.1147 degrees for longitude. Vertically, a z-grid
 161 (Losch et al., 2010) with 50 levels is used. The model bathymetry comes from the BEDMAP2
 162 dataset (Fretwell et al., 2013), but is complemented with data from the General Bathymetric
 163 Chart of the Oceans (GEBCO, www.gebco.net) north of 60°S, which is the northern extent of
 164 BEDMAP2.
 165



166
 167 Figure 1: a) Model bathymetry with the region of Palmer-LTER cruises marked in the red rectangle and b) locations of the
 168 Palmer-LTER stations. Orange dots represent coastal stations, blue dots represent shelf stations, and red stars represent slope
 169 stations. The transect lines in the southern region are lines 200 (southernmost) and 300, and the transect lines in the northern
 170 region are 400, 500 and 600 (northernmost). Sub-regions analyzed are named northern coastal (n_cs), northern shelf (n_sh),
 171 northern slope (n_sl), southern coastal (s_cs), southern shelf (s_sh) and southern slope (s_sl).
 172

173 2.2 Initial and Boundary conditions, and surface forcing

174

175 The initial conditions for temperature and salinity were obtained from the World Ocean
 176 Atlas (WOA, Boyer et al., 2009). The model has three open boundaries (north, east and west)
 177 with prescribed monthly mean ocean temperature, salinity and velocity, as well as sea-ice
 178 concentration, thickness and velocity obtained from a large-scale, low-resolution circumpolar
 179 MITgcm simulation (Holland et al., 2014). Sea-ice velocities are not prescribed at the
 180 boundaries to avoid spurious ice convergence. The atmospheric forcings are obtained from the
 181 ERA-Interim reanalysis (Dee et al., 2011) with a horizontal resolution of 1.5° in latitude and

182 longitude and a 6-hour interval. Although ERA-Interim has been found to be the most reliable
183 reanalysis for some atmospheric parameters (Bracegirdle and Marshall, 2012), it is also known
184 that most reanalyses, including ERA-Interim, underestimate moderate to high wind events.

185 As this model was originally used to study freshwater distribution in the Bellingshausen
186 Sea, the freshwater inputs were carefully chosen to be as realistic as possible, given the
187 constraints imposed by lack of data (Regan et al., 2018). A general surface runoff input was
188 imposed to represent surface melt of land-based ice, and iceberg calving and melting. Values of
189 the total surface runoff are chosen to represent the amount estimated by Van Wessem et al.
190 (2016), and they are distributed uniformly along the coast and linearly decreasing with distance
191 from land out to 100 km. Different from the steady freshwater input used in Regan et al.
192 (2018), this study introduces a seasonal cycle of the freshwater input with greater values in
193 summer and smaller values in winter. The annual mean glacial input was multiplied by a cosine
194 anomaly in time, which gives a different value for each month and maintains the total input
195 amount over the course of a year.

196

197 2.3 Parameterization of Langmuir Circulation

198 The model uses the K-profile parameterization (KPP; Large et al., 1994) to parameterize
199 sub-grid scale vertical turbulence in the surface boundary layer and ocean interior, and here we
200 consider the influence of LC in the KPP framework as an enhancement factor to the turbulence
201 velocity scale used for the surface boundary layer. The time scale of ocean surface layer
202 responding to winds, forming surface waves, and establishing/dissipating Langmuir vortices is
203 relatively short (Talley et al., 2011). The impact of LC on mixing and surface MLD could thus be
204 considered by directly coupling surface wave models with atmospheric conditions. However,
205 direct simulation of the ocean surface waves over the spatial and temporal scale of our
206 interests is computationally prohibitive, and there is limited data for validating wave models in
207 the Southern Ocean. For this reason, this study employs empirical wave spectra, following Li et
208 al. (2017), to estimate the surface wave conditions using winds at 10 m above sea surface.

209 Two approaches of including LC, based on the parameterizations of Li et al. (2017) and Li
210 and Fox-Kemper (2017), respectively, are tested here. The approach described in Li and Fox-
211 Kemper (2017) parameterizes the influence of LC in the entrainment of dense water from
212 below the mixed layer. Two main factors affecting the rate of entrainment, i.e., entrainment
213 buoyancy flux, $\overline{w'b'_e}$, are i) destabilizing surface buoyancy flux, important in convective
214 turbulent regimes and ii) shear instability at the base of the surface mixed layer, dominant
215 under wind-driven regimes. The latter factor is often associated with processes such as inertial
216 oscillations of the surface current. Here, w' is vertical turbulent velocity anomaly, and b' is
217 buoyancy fluctuation. When both factors are present, a proportionality is assumed and a new
218 velocity scale, w_x , combining convective velocity scale and water-side friction velocity (Large et
219 al., 1994), is introduced. w_x relates to the rate of entrainment so that:

$$\overline{w'b'_e} = -0.2 w_x^3 / h_b$$

220 (Equation 1)

221

222 where h_b is the boundary layer depth and is defined as the smallest depth at which the bulk
223 Richardson number,

$$Ri_b(z) = \frac{|z|[b_r - b(z)]}{|u_r - u(z)|^2 + U_t^2(z)}$$

224 (Equation 2)

225 reaches a critical value of 0.3. Here, u_r is a reference speed, u is water speed, b_r is a reference
226 buoyancy, b is buoyancy, and U_t is a velocity scale that accounts for the influence of subgrid
227 velocity and shear. Several large-scale eddy simulations (e.g., Grant and Belcher, 2009;
228 McWilliams et al., 2014) have suggested that $\overline{w'b'_e}$ is enhanced in the presence of LC. This
229 would happen because LC enhances turbulent kinetic energy (TKE) at the base of the mixed
230 layer. Langmuir turbulence could also contribute to the erosion of the thermocline through
231 enhancing shear instability beneath the downwelling regions of the LC cells. However,
232 quantifying the Langmuir enhanced $\overline{w'b'_e}$ is nontrivial due to small magnitude of the TKE
233 budget as a whole.

234 The solution proposed by Li and Fox-Kemper (2017) includes the introduction of a new
235 velocity scale, U_t , based on the surface turbulent Langmuir number:

236

$$U_t(z) = \frac{C_v N(z) w_s(z) |z| \left[\frac{-\overline{w'b'_e} h_b}{w_s(z)^3} \right]^{-1/2}}{Ri_c}$$

$$= \frac{C_v N(z) w_s(z) |z| \left[\frac{0.15 w^{*3} + 0.17 u^{*3} (1 + 0.49 La_t^{-2})}{w_s(z)^3} \right]^{-1/2}}{Ri_c}$$

237 (Equation 3)

238 where N is the local buoyancy frequency, w_s is the turbulent velocity scale, C_v is a defined
239 parameter based on buoyancy, u^* is the magnitude of frictional velocity, Ri_c is the critical
240 Richardson number, La_t is the turbulent Langmuir number:

$$La_t = \sqrt{u^* / u_0^s}$$

241 (Equation 4)

242 and u_0^s is the Stokes drift speed, which is the average speed of a specific fluid parcel over
243 multiple wave periods. While the Stokes drift is not calculated by the model, it is dependent on
244 the high-frequency part of the wave spectrum, which is reasonably well described by the
245 empirical wave spectra. The wave spectra used to calculate the Stokes drift is based on the
246 Phillips spectrum (Phillips, 1985), and the directional spreading of wind waves of Webb and
247 Fox-Kemper (2015) is also considered. In the calculation of wave spectra, the peak frequency is

248 often assumed to be related to the wind speed, so that the wind speed at 10 m height is used
249 for this calculation.

250 The second approach tested in this study, based on the work of Li et al. (2017),
251 represents Langmuir turbulence as an enhancement factor applied to the turbulent velocity
252 scale used in the KPP formulation. The idea of an enhancement factor had already been
253 presented by McWilliams et al. (2000), whose enhancement factor is a function of La_t .
254 However, the formulation proposed by McWilliams et al. (2000) introduces spurious extra
255 mixing in the extra-tropical regions, possibly because it does not include wind-wave
256 misalignment. The parameterization of Li et al. (2017) uses a theoretical wave model based on
257 the Stokes drift profile, the boundary layer depth and the surface friction velocity (see equation
258 25 of Li et al., 2017):

$$\varepsilon = f(u_{10}, u^*, h_b)$$

260 (Equation 5)

261 where u_{10} is the wind velocity at 10-meters height. The boundary layer depth and surface
262 friction velocity are provided by the model, and the Stokes drift is calculated as previously
263 explained.

264 Both parameterizations of LC depend on wind speed and assume direct work of wind on
265 the ocean surface. However, the presence of sea ice modifies ocean surface waves and the air-
266 ocean drag, which in turn modifies the surface momentum exchange (Andreas et al., 1984;
267 Birnbaum and Lüpkes, 2002). The efficiency of wind inducing Stokes drift thus varies with sea-ice
268 concentration (SIC). Here, to consider the influence of sea ice on the wind work, we seek to
269 introduce a coefficient to the 10-m wind speed. While there are no data or concrete formula to
270 describe the change of wind work around sea ice, a study by Andreas et al. (2010) using data
271 collected in the Arctic over a year-long experiment proposes a relationship between SIC and Cd ,
272 the drag coefficient of the friction between 10-m wind and ocean:

$$10^3 Cd = 1.5 + 2.233 \times SIC - 2.333 \times SIC^2$$

274 (Equation 6)

275 It is seen from this equation (plotted on supplemental material) that Cd is enhanced at
276 intermediate SIC. This can be explained by the fact that at low to intermediate SIC ice floes will
277 have higher pressure in the upwind and lower pressure in the downwind face, essentially
278 functioning like a sail, which enhances the wind work. At high SIC, ice floes shelter each other
279 and decrease the momentum transfer from air to the ocean. Since frictional velocity is
280 proportional to Cd , we assume that the quadratic dependence of Cd on SIC can be translated to
281 the dependence of Stokes velocity on SIC. Therefore, we derived an equation for an
282 enhancement factor (s_c) dependent on SIC to be multiplied by the wind velocity, U_{10} , and
283 account for increased momentum transfer at intermediate SIC:

284

$$s_c = 1 + 2 \times SIC - 3 \times SIC^2$$

285

(Equation 7)

286 so that s_c (plotted against SIC in supplemental material) equals one in the absence of sea ice
287 (no enhancement), peaks at intermediate concentrations and at a rate similar to the Cd
288 enhancement ($\sim 35\%$), and is zero when SIC approaches one (no Langmuir influence in areas
289 completely covered by sea ice due to absence of ocean surface waves). There are great
290 uncertainties in this relationship between wind influence and SIC, and the uncertainties are at
291 the moment impossible to be clarified due to the lack of data. Nevertheless, we assume this
292 approach of considering sea ice influence on the LC is more realistic than using a linear
293 relationship between wind influence and SIC.

294

295

2.4 Description of experiments

296

297 Hindcast simulations were integrated between 1984 and 2014, with 1984 to 1990
298 considered spin-up. Therefore, the model period analyzed covers the period from the beginning
299 of the Palmer-LTER field measurements (1991 onwards, see section 2.5) until 2014. The model
300 output consists of daily averages of the ocean and sea-ice variables. The study examines four
301 simulations with different parameterizations for LC and different values for air-sea-ice drag
302 coefficient, Cd (Table S1 on supplemental material).

302

303 The value of Cd is linked to the characteristics of sea ice and shows a wide range of
304 values in both observational and modeling studies, ranging from 5×10^{-4} to $>3 \times 10^{-3}$ (e.g.
305 Wamser and Martinson, 1993; Castellani et al., 2014; Miller et al, 2006; Tsamados et al., 2014).
306 The value used in Regan et al. (2018) was 5×10^{-4} , on the lower end of Cd estimates. The choice
307 of using a low Cd value was intended to adjust the formation of polynyas around Eltanin Bay
308 (south of the Palmer-LTER region) and the freshwater fluxes around George VI Ice Shelf.
309 Lowering the drag coefficient also lowers the impact of wind in transporting sea ice to different
310 regions, hence curbing the formation of polynyas. For the Palmer-LTER region, however, a
311 lower drag coefficient means that more sea ice could be melted locally rather than be
312 transported elsewhere, thus lowering the surface salinity and increasing stability in coastal and
313 shelf regions. Therefore, Cd values of 5×10^{-4} and 2×10^{-3} (on the higher end of the observed
314 values) were used in different simulations to assess the impact of sea-ice transport in local
315 surface ocean mixing and freshwater budget.

315

316 In the control simulation (CTRL), $Cd = 2 \times 10^{-3}$ and the parameterization for LC is based
317 on the entrainment buoyancy flux (Li and Fox-Kemper, 2017). Sensitivity simulation LowCd has
318 a similar configuration to CTRL, but with $Cd = 5 \times 10^{-4}$. To assess the effect of different
319 parameterizations for LC, sensitivity simulations without any LC parameterization (NoLC) and
320 with the LC parameterization based on an enhancement factor for wind mixing (EnhLC; Li et al,
2017) are carried out. All other parameters in NoLC and EnhLC are the same as in CTRL.

321
322
323
324
325
326
327
328
329
330
331
332
333
334
335
336
337
338
339
340
341
342
343
344
345
346
347
348
349
350
351
352
353
354
355
356
357
358

3 Data used for skill assessment

The Palmer-LTER project started in 1991 and has been collecting a range of physical, biological and chemical data along the WAP since, including semiweekly water-column sampling from Palmer Station from October through March each year and an annual cruise each January-February since 1993 (Ducklow et al., 2013). Given that the data collected at Palmer Station are highly influenced by local phenomena, such as the passage of icebergs, that are not captured by the model, they are excluded in the model validation and analysis.

The cruise data used for model validation are from lines 200 to 600 of the Palmer-LTER grid, spanning an area of 500 km along the coast and 250 km across the shelf. The cross-shelf transects are spaced every 100 km in the along-shelf direction, and the stations on each transect are separated by 20 km (figure 1b). All the data collected are available through the project web page (<http://pal.lter.edu/data/>). Modeled vertical profiles of salinity and temperature are compared to the cruise CTD (conductivity, temperature and depth) profiles. It is important to note, however, that not all stations are sampled every year.

Each individual CTD cast does not necessarily reflect the mean state of the water column during the summer of data collection due to the influence of synoptic processes. In order to decrease the influence of short-term and small-scale processes on the CTD casts during the analyses, the cruise data are divided in north (lines 400, 500 and 600) and south (lines 200 and 300) regions (Figure 1b), and also into coastal, shelf and slope regions, based on topography. This way, 6 different sub-regions are obtained: north coastal (n_cs), north shelf (n_sh), north slope (n_sl), south coastal (s_cs), south shelf (s_sh) and south slope (s_sl).

Onset time of sea-ice advance and retreat are obtained from the GSFC (Goddard Space Flight Center) Bootstrap algorithm (Comiso, 2017). The sea-ice year starts in mid-February, from day 46 of the calendar year until day 410. SIC refers to the percentage of each cell area covered by sea ice, ranging from zero (no sea-ice cover) to one (totally covered by sea ice). Onset time of sea-ice advance is chosen to be the day in which the average SIC of all the stations in each Palmer-LTER grid sub-region reaches at least 0.15 for 5 days in a row. Onset time of sea-ice retreat is calculated as the last day in which SIC is less than 0.15 for the sea ice season. Further details are provided in Stammerjohn et al. (2008; 2012). The sea-ice data used to calculate the climatological SIC for each sub-region is from the same source, and binned as 8-day means with horizontal resolution of 0.2 degrees in both latitude and longitude. For surface freshwater content, oxygen isotope data, described in Meredith et.al. (2008, 2010, 2013) was the primary dataset used for the model skill assessment.

359 4 Results

360

361 To compare the model results with the Palmer-LTER cruise data, values at model grid points
362 closest to Palmer-LTER stations are analyzed. Following Mitchel and Holm-Hansen (1991), we
363 use the threshold of density change of 0.05 kg/m^3 over a 5-meter interval to define surface
364 MLD. Onset times of sea-ice advance and retreat in the model data were calculated as per the
365 observational data.

366 As a first assessment of the skill of the model in reproducing the broad seasonal
367 patterns observed in the surface ocean in the WAP region, we examine summer (December to
368 February) and winter (June to August) climatological surface salinity, temperature, currents and
369 SIC in Simulation CTRL (figure on supplemental material). The main circulation pattern in the
370 WAP region is a northeastward current of the ACC along the shelf break, which is present in the
371 model results. The horizontal resolution of the model is not sufficient to properly resolve the
372 coastal circulation, described in Moffat and Meredith (2018), however the outputs do capture
373 the cross-shelf flows described in the same study. The modeled sea surface temperature (SST)
374 shows an onshore-offshore gradient during the summer, with colder waters on the shelf where
375 sea ice has recently melted, as well as a latitudinal gradient with colder waters towards the
376 southern part of the domain. During the winter, SST values reflect the sea-ice freezing
377 temperature near the coast and shelf region in most of the area.

378 Simulation CTRL captures an onshore-offshore gradient in summer surface salinity with
379 lower salinities reaching minimums of around 32.5 near the coast, as described in the literature
380 (Meredith et al., 2017). While a salinity gradient is present in the winter in the southern part of
381 the model domain, it is not as marked as during the summer months, when sea-ice melt and
382 increased glacial input contribute to lowering the salinity near the coast. Sea ice extends past
383 the shelf break during the winter and is confined to the region south of Marguerite Bay during
384 the summer. Overall, seasonal variations of the surface variables in Simulation CTRL match the
385 main patterns captured by the observations.

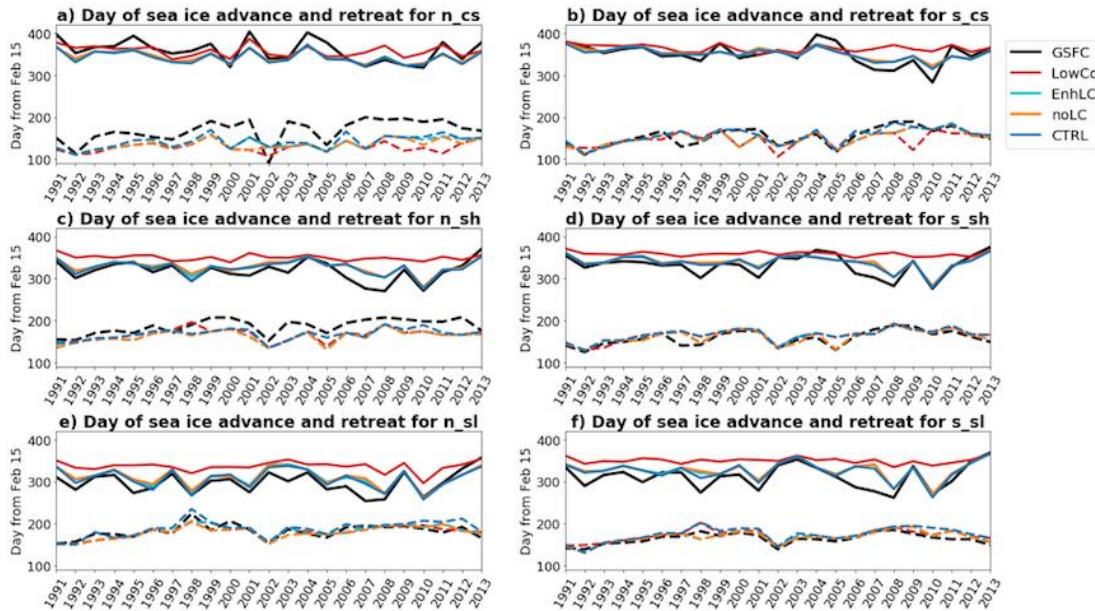
386

387 4.1 Sea-ice advance and retreat

388

389 To assess how well the model captures sea ice interannual variability, modeled onset
390 times of sea ice advance and retreat over the simulation period are plotted against the
391 observations (Figure 2). Correlation coefficients between modeled and observed onset times of
392 sea-ice advance and retreat for each sub-region are calculated (Tables S2 and S3 on
393 supplemental material). When comparing the results of the CTRL simulation with the
394 observations, it is seen that sea-ice advance is well represented in the model in the southern
395 region, while in the north the model shows earlier advance in the coastal and shelf areas. For
396 sea-ice retreat, the CTRL run performs better in the shelf and slope regions than in the coastal

397 regions. In the northern coastal region, the model shows earlier retreat than the observations
 398 in most years, and while in the southern coast the model was able to capture the timing of sea
 399 ice retreat observed, years of early (2006, 2007, 2010) and late (2004) retreat were not well
 400 represented.
 401



402
 403 Figure 2: Evolution of the onset times of sea ice advance (dashed line) and retreat (solid) in sub-regions northern coastal (a),
 404 southern coastal (b), northern shelf (c), southern shelf (d), northern slope (e) and southern slope (f). Black lines represent
 405 results for satellite observations, and other lines represent results from different simulations.
 406

407 Wind action has a larger influence in the timing of sea-ice advance and retreat than LC,
 408 evidenced by the larger difference between the CTRL and LowCd results compared to the
 409 difference between CTRL and EnhLC/noLC. The comparison simulations suggest that wind
 410 action has a larger influence on the retreat of sea ice than on the advance. This likely reflects
 411 the fact that sea ice advance is driven more by thermodynamics rather than mechanical forcing.
 412 The influence of LC on sea-ice advance/retreat was much more modest and mainly consisted of
 413 small differences in the onset time of sea-ice advance. Without any parameterization for LC
 414 (NoLC) sea ice advances slightly earlier in the coastal areas, and in the slope region in some
 415 years.

416 Interannual variability of the timing of sea-ice advance and retreat also seem to be more
 417 influenced by wind action than by representation of LC. The correlations between modeled and
 418 observed sea-ice advance and retreat show that the CTRL simulation has better representation
 419 of interannual variability, with correlation coefficients mostly higher than 0.8, with the
 420 exception of sea-ice advance in the northern coast (0.62) and shelf (0.70) regions. The
 421 coefficients calculated for experiments EnhLC and NoLC were similar to those of the CTRL run,
 422 and LowCd had the lowest correlations for both sea ice advance and retreat.

423 In summary, the choice of wind-sea-ice drag coefficient has a larger impact in the
424 representation of seasonal and interannual sea-ice cycles than the inclusion of LC, with low
425 drag leading to higher SIC and delayed sea-ice retreat. While sea-ice retreat seems to be highly
426 affected by wind influence on sea ice, differences in sea-ice advance do not seem to be related
427 to wind in all regions except for northern coastal, and are likely more affected by changes in
428 surface salinity and temperature between the simulations. Biases in atmospheric forcing
429 (particularly wind forcing) might play a role in the disparities found between the models and
430 observations in some years, and their exact contribution and the associated mechanism are
431 unclear and left for future studies.

432

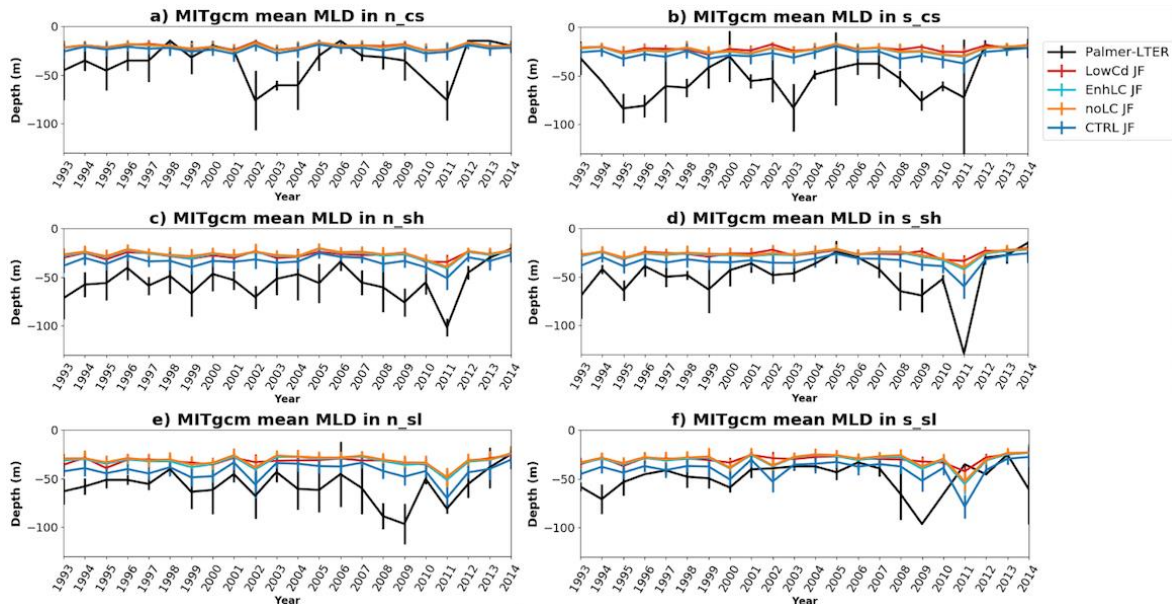
433 4.2 Surface Mixed Layer Depth (MLD)

434

435 4.2.1 Variability of Summer MLD

436 In order to compare the model results to the Palmer-LTER CTD cruise data, simulated
437 daily MLD in each sub-region in the months of January and February are averaged for each
438 year. The results are compared to the observed mean MLD in each sub-region for each cruise
439 (Figure 3). The choice of using the modeled mean MLD in January and February was made
440 because January and February are the months in which the cruises (which last about 6 weeks)
441 take place. Comparing the results on individual dates would not necessarily improve the model-
442 observation comparison, since small scale phenomena such as passage of submesoscale
443 features and icebergs or a locally-strong wind might affect the MLD at each individual station,
444 and these phenomena are not captured by the model. However, with a long enough dataset,
445 and using data from different stations, the Palmer-LTER cruise data should be able to represent
446 the interannual variability of MLD in the WAP to some degree at regional scale.

447 The CTRL simulation gives mean MLD shallower than observed throughout the domain.
448 The difference between model and observations is particularly large in the southern coastal and
449 northern shelf regions. Although less variation is expected in the modeled MLD, given it is
450 represented as a 2-month average, it also shows lower standard deviation (calculated from
451 daily values). However, the interannual variability in the CTRL simulation seems to be
452 reasonably well represented in most of the domain, with correlation with observation greater
453 than 0.93 in the southern shelf. Modeled MLD variability is less representative in the northern
454 coastal (correlation = 0.308) and southern slope (correlation = 0.110) regions. The low
455 correlation in the northern coast is expected as MLD in the coastal region is influenced by local
456 phenomena that are not well captured by the model. It is not clear why the southern slope fails
457 to capture interannual variability. A possibility is that the southward advection of sea ice during
458 the retreat is less pronounced in the model compared to observations, which would affect the
459 amount of melt in the southern slope. Although there is limited data on sea-ice thickness, it is
460 also possible that it is overestimated in the model.



462
 463 Figure 3: Averaged mixed layer depth (MLD) for January and February each year from the Palmer-LTER cruise (black lines) and
 464 from the simulations (other colors). For the model data, vertical lines indicate the standard deviation of the data considered in
 465 each sub-region and year; for the Palmer-LTER data, vertical lines represent the standard deviation of the data in each sub-
 466 sub-region for each cruise. Data are shown for northern coast (a), southern coast (b), northern shelf (c), southern shelf (d), northern
 467 slope (e) and southern slope (f).

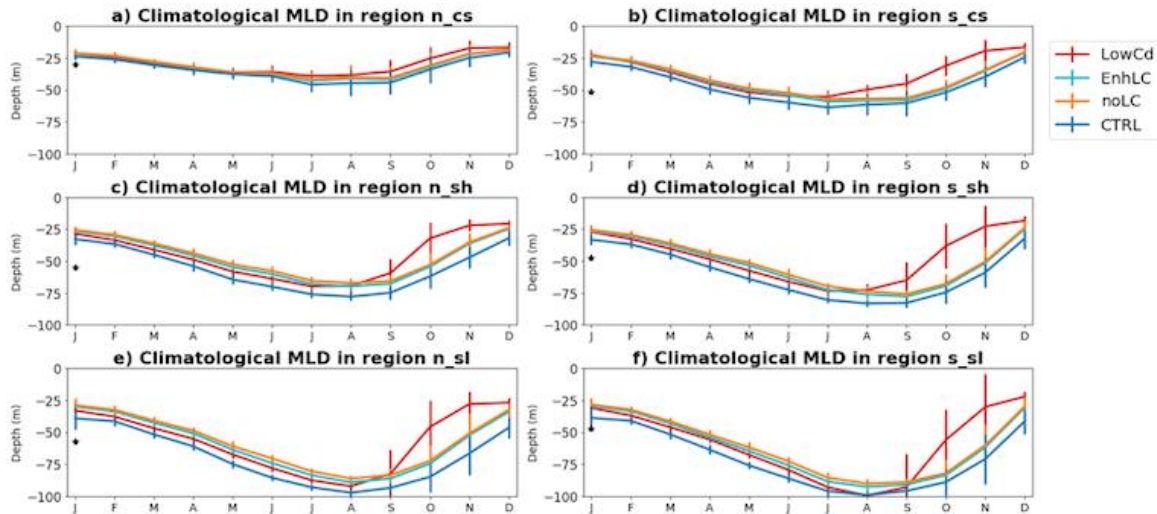
468
 469 The CTRL simulation had the deepest MLD among all the sensitivity simulations. Despite
 470 having the same parameterization for Langmuir circulation as CTRL, LowCd MLD was mostly
 471 similar or shallower than NoLC and EnhLC, implying that properly representing wind-sea-ice
 472 drag in the model has as much or more influence on MLD as properly representing Langmuir
 473 circulation. Between the two approaches to parameterizing LC, entrainment from the bottom
 474 of the mixed layer (CTRL) had a larger impact than applying an enhancement factor (EnhLC).

475 Overall, the CTRL simulation had better performance in simulating both the depth and
 476 interannual variability of the mixed layer, although a bias towards shallow MLD still persists.
 477 This indicates that both using a higher drag coefficient and including LC parameterization based
 478 on entrainment buoyancy flux are important for resolving the MLD, but properly simulating the
 479 sea-ice cycle as well as capturing the redistribution and volume of sea ice melt have a bigger
 480 impact in reproducing the interannual variability of the MLD.

481 482 4.2.2 MLD seasonality

483 Although seasonality of MLD is hard to validate due to lack of data during the cold
 484 months of the year, it is known that MLD deepens during the winter due to surface cooling,
 485 formation of sea ice and subsequent brine rejection. Comparisons between the seasonal cycle
 486 of MLD in the different model simulations were made to investigate how the changes made to
 487 the model parameters affect MLD throughout the year. For that purpose, the monthly

488 climatology of MLD for each sub-region was plotted for all model simulations (Figure 4).
 489 Immediately apparent from the figure is that the CTRL simulation has deeper MLD throughout
 490 the year and in all sub-regions, with maximum depth being reached in August and deeper MLD
 491 farther away from the coast.
 492



493
 494 Figure 4: Simulated monthly climatologies of MLD in northern coast (a), southern coast (b), northern shelf
 495 (d), northern shelf (c), southern shelf (d), northern slope (e) and southern slope (f) regions. The black star in January represents the average observed MLD for each
 496 region, calculated using the Palmer-LTER cruise data.
 497

498 LowCd has consistently shallower MLD, except for the month of August in the southern
 499 slope region. The difference between these two simulations is more accentuated during the
 500 spring and early summer, when LowCd overestimates SIC (supplemental material). Shallower
 501 MLD in LowCd occurs even in areas and months in which sea ice is absent and both simulations
 502 would have similar physics. Regarding the different parameterizations of LC, applying the
 503 enhancement factor (EnhLC) only seems to deepen the mixed layer during the fall and winter in
 504 the slope regions, when the difference between EnhLC and noLC is visible but smaller than 5
 505 meters. The parameterization used in the CTRL simulation, based on entrainment from below
 506 the mixed layer, deepened the MLD throughout the domain with the exception of summer and
 507 fall in the northern coast. From the results, we conclude that increased SIC during the spring
 508 and summer will shoal the MLD during these seasons, and in this case a shallower MLD can also
 509 be seen during fall and winter in most regions. Properly simulating sea-ice retreat, therefore, is
 510 important for the simulated MLD year-round.
 511

512 4.3 Vertical structure of the water column

513 The water mass distribution in the surface and subsurface layers of the WAP are marked
 514 by the presence of Antarctic Surface Water (AASW), Winter Water (WW) and Circumpolar Deep
 515 Water (CDW), respectively, and have been described in several studies (e.g. Klinck et al. ,2004;

516 Moffat et al., 2008; Moffat and Meredith, 2018). CDW is a subsurface water mass derived from
517 the Antarctic Circumpolar Current (ACC), which flows close to the shelf break at the WAP,
518 sporadically intruding onto the shelf. CDW is comparatively warm, with temperatures higher
519 than 1°C, and nutrient rich, playing an important role for primary production. CDW is modified
520 as it flows across the shelf, cooling linearly with distance towards the coast. Above the CDW is
521 the WW, which is formed by deep mixing from brine rejection during winter sea ice production,
522 which then becomes isolated (forming 'remnant WW') from the surface by summer
523 stratification. The summer surface stratification is due to increased heat input from solar
524 radiation and freshening during sea-ice melt and glacial discharge from land, forming the
525 AASW, which consequently traps the remnant WW between the AASW and the modified CDW,
526 and is represented by a cold layer (temperatures below 1°C) located between 80 to 100 meters.

527 The mean January/February salinity and temperature profiles of each model experiment
528 were plotted for each sub-region along with the average Palmer-LTER cruise profile (Figure 5 for
529 northern region and Figure 6 for southern). The August averages for each experiment are also
530 plotted to represent the winter water column (supplemental material). The vertical profiles of
531 the CTRL simulation have lower surface salinity and higher surface temperature when
532 compared with the summer observations, which is consistent with late and increased sea-ice
533 melt. An increased amount of meltwater would lower surface salinity and increase the stability
534 of the surface layer. With a more stable surface layer, heat from the atmosphere is distributed
535 over a shallower depth, increasing the surface temperature and further increasing the stability
536 of the mixed layer. In the observations, a deeper mixed layer leads to lower surface
537 temperature not only because surface heat is distributed deeper, but also because more WW is
538 entrained from below.

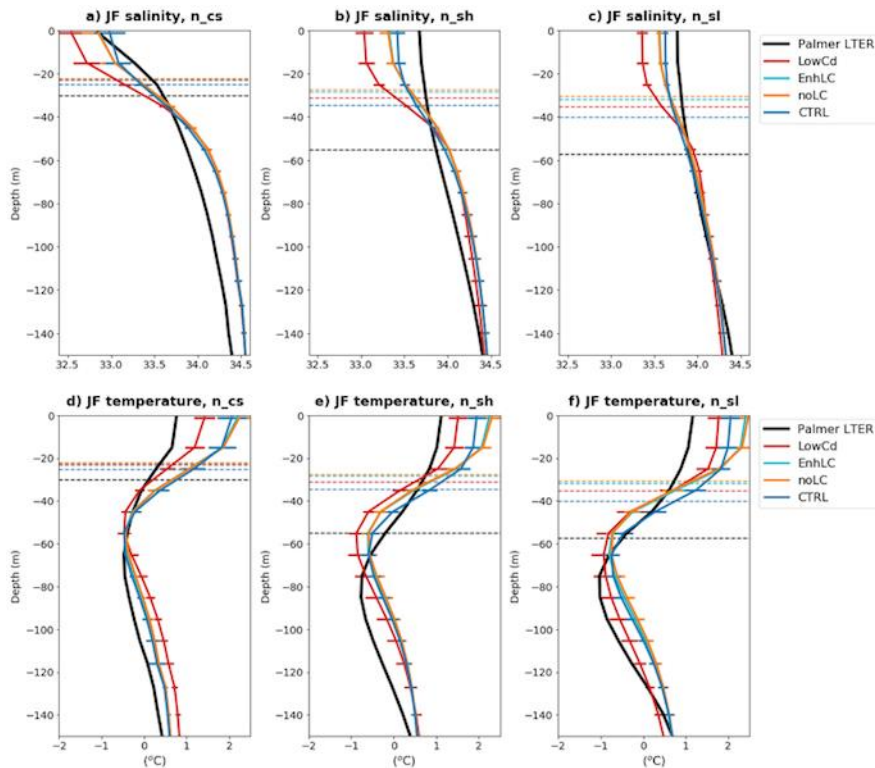
539 Compared to the CTRL simulation, LowCd has lower surface temperature and salinity
540 during the summer, likely because sea-ice retreat happens later in LowCd. New meltwater on
541 the surface tends to be cold prior to gaining heat through insolation. Although LowCd brings the
542 surface temperature closer to observations when compared to CTRL, this likely happens for the
543 wrong reason: due to late sea-ice retreat, instead of deeper mixing. During the winter, salinity
544 profiles are similar between the simulations in the slope region, but LowCd shows lower surface
545 salinity in the coast and shelf.

546 At the surface, the simulation with no LC shows higher temperature and lower salinity in
547 the summer compared to CTRL, increasing the differences from the observations and
548 confirming the positive impact of buoyancy flux entrainment-based LC parameterization on
549 properly simulating the surface ocean layer. Using the enhancement factor to parameterize LC
550 (EnhLC) had similar results to the simulation with noLC. The only difference observed between
551 EnhLC and noLC during the summer is a slightly lower salinity close to the surface in EnhLC.
552 Although EnhLC had larger impact on vertical salinity and temperature during the winter when

553 compared to noLC, the effect of the enhancement factor was still smaller than the
554 parameterization included in the CTRL simulation.

555 The differences observed in MLD and vertical profiles among the simulations suggest
556 that the influence of late and increased sea-ice melt in the coastal and shelf region during the
557 summer persists throughout the year, with lower surface salinity and shallower mixed layer
558 observed during the winter. On the slope, winter MLD is more impacted by the choice of LC
559 parameterization than by the choice of drag coefficient.

560



561

562 Figure 5: Simulated January-February climatology and Palmer-LTER cruise climatology of salinity for (a) northern coast, (b)
563 northern shelf and (c) northern slope regions; and simulated January-February climatology and Palmer-LTER cruise climatology
564 of temperature for (d) northern coast, (e) northern shelf and (f) northern slope regions. Horizontal solid lines represent
565 standard deviation, and horizontal dashed lines indicate climatological MLD for the period considered.

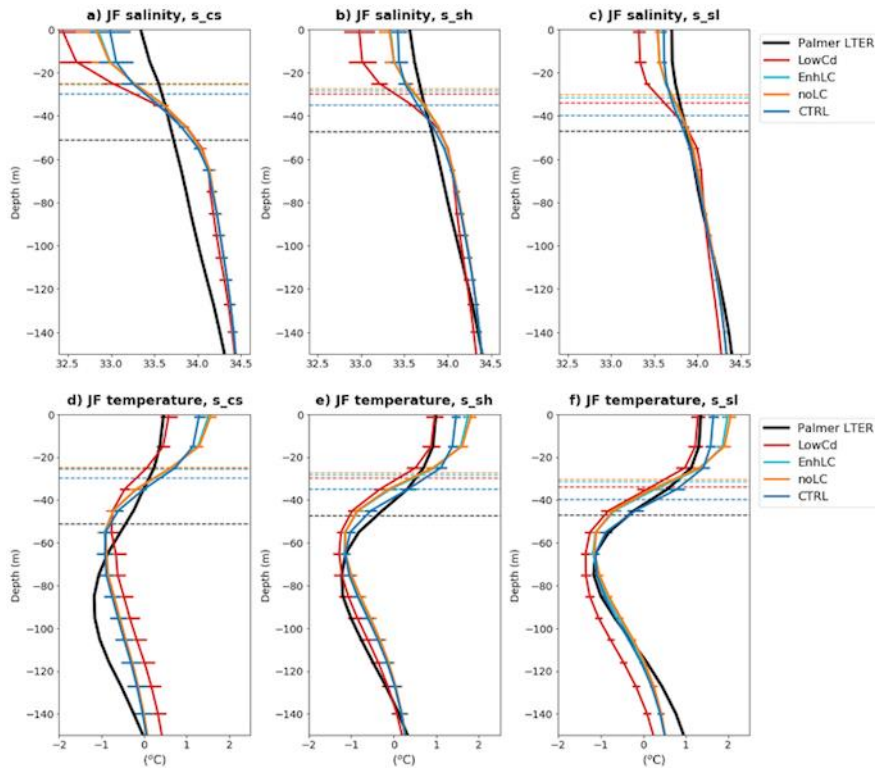
566

567

568 4.4 Freshwater seasonality

569 The freshwater cycle in the WAP has an important role for the coastal circulation
570 (Moffat et al., 2008; Moffat and Meredith, 2018) and for primary production. Glacial meltwater,
571 in particular, is thought to be a major source of dissolved iron (Annett et al., 2017), which is
572 likely the limiting nutrient in the WAP given that nitrogen and silica are rarely depleted (Kim et
573 al., 2016). Studies aimed at quantifying the amount and source of freshwater in the WAP
574 surface ocean have been conducted using oxygen isotope data (Meredith et al., 2008; 2013;
575 2018) to identify whether the freshwater is derived from sea-ice melt or from meteoric sources,

576 which is derived from the atmosphere and includes precipitation and glacial melt. Although sea-
 577 ice formation and melt does not represent a net input of freshwater if integrated over a full
 578 season and over a large enough region, an excess of sea-ice melt (formation) can be a source
 579 (sink) of freshwater at certain locations due to the redistribution of sea ice (i.e., by winds) from
 580 the location where in situ growth occurred.
 581



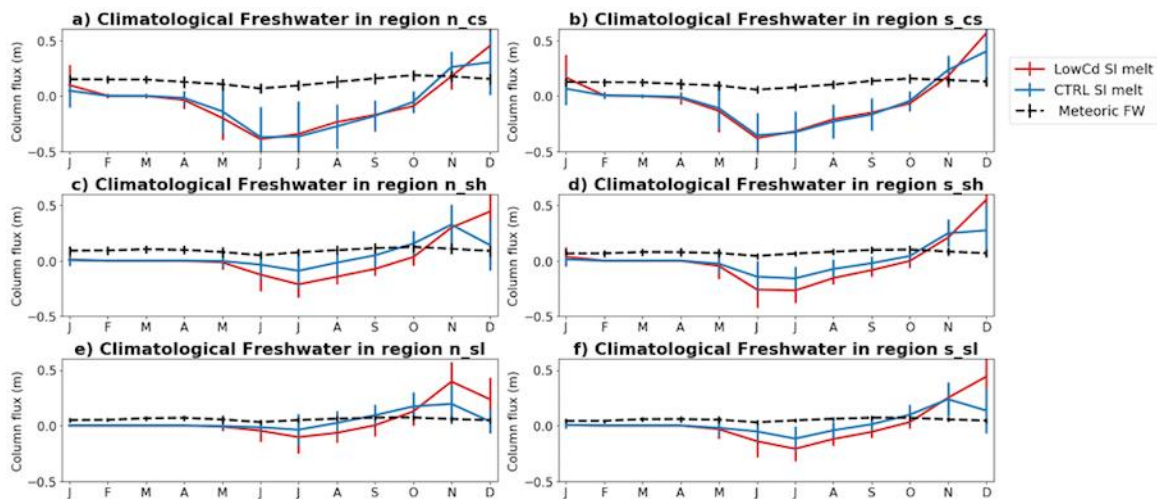
582
 583 Figure 6: Simulated January-February climatology and Palmer-LTER cruise climatology of salinity for (a) southern coast, (b)
 584 southern shelf and (c) southern slope regions; and simulated January-February climatology and Palmer-LTER cruise climatology
 585 of temperature for (d) southern coast, (e) southern shelf and (f) southern slope regions. Horizontal slide lines represent
 586 standard deviation, and horizontal dashed lines indicate climatological MLD for the period considered.
 587

588 Since the oxygen isotope samples were collected during the Palmer-LTER cruises in
 589 January and February, the spatial and temporal patterns of freshwater distribution derived
 590 from these data represent the summer distribution only. Given the model used in this study has
 591 a reasonable representation of the sea-ice cycle and includes seasonality in the discharge of
 592 glacial freshwater, the results can be used to estimate the influence of different sources of
 593 freshwater throughout the year. However, because there is no interannual variability in the
 594 glacial runoff in the model, the analysis is restricted to the seasonal climatology of freshwater.
 595

596 From the cruise observations in late summer, it is seen that there is a cross-shelf
 597 gradient in salinity, with lower salinities around 33.2 near the coast coinciding with higher
 598 concentrations of meteoric water (Meredith et al., 2013). Although meteoric water has a highly
 variable and heterogeneous spatial distribution, cruise measurements indicate that it is the

599 dominant source of freshwater across the shelf in most years. Sea-ice melt concentrations in
 600 the near surface were highly variable from year to year (Meredith et al., 2017). Despite the
 601 high variability, the data also suggests that there is more sea-ice formation towards the north
 602 and more sea-ice melt towards the south of the WAP. Sea-ice formation, however, leads to
 603 deepening of the mixed layer, and the isotopic signature associated with this process also gets
 604 mixed downward in the water column during this process. Accordingly, there is a seasonal
 605 asymmetry in the vertical distribution of isotope-derived freshwater prevalences, which adds
 606 complexity to the interpretation of these data (Meredith et al., 2013).

607 To analyze the seasonality of the modeled freshwater sources in the different sub-
 608 regions, modeled climatological monthly means for sea-ice melt and meteoric freshwater are
 609 plotted for CTRL and LowCd (Figure 7), with positive values indicating addition of freshwater by
 610 sea-ice melt and negative values indicating sea-ice formation. The results of EnhLC and NoLC
 611 are not included in the figure because the sea ice cycle in those simulations is very similar to the
 612 CTRL simulation. Also, only one line is represented for meteoric freshwater, the sum of
 613 precipitation and glacial runoff, because the value is the same for all the simulations.
 614



615
 616 Figure 7: Monthly climatologies of sea ice meltwater (color) from Simulations LC (blue) and LC_Cd (red), and monthly
 617 climatology of simulated meteoric freshwater from the simulations (black) in northern coast (a), southern coast (b), northern
 618 shelf (c), southern shelf (d), northern slope (e) and southern slope (f) regions. Vertical lines represent the standard deviation.
 619

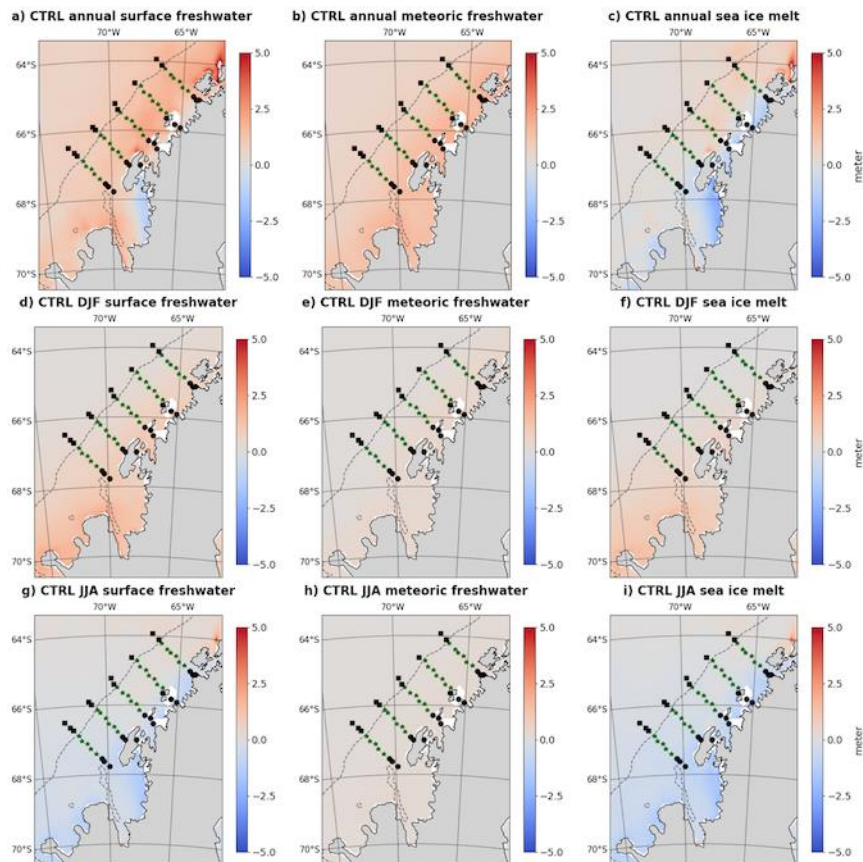
620 It is seen that although a strong seasonal cycle is included in the glacial runoff, with
 621 increased discharge during the summer, seasonality in overall meteoric freshwater input is
 622 dampened by the precipitation in the atmospheric forcing. Meanwhile, a pronounced seasonal
 623 cycle exists in the sea-ice melt. The CTRL results for sea-ice melt indicate that it is the dominant
 624 freshwater source between October and December in some sub-regions. Towards the end of
 625 the summer meteoric water is present in higher concentrations throughout the whole domain,
 626 in accordance with the observations. CTRL results also show that most of the sea ice formation
 627 happens in the coastal region during the winter. Despite melt seasonality being different for

628 each sub-region, the overall summer melt, as indicated by the sum of sea-ice melt from
629 October to February, is larger in the southern region for coastal (0.6 m north, 0.7 m south),
630 shelf (0.47 m north, 0.53 m south) and slope (0.23 m north, 0.37 m south) stations, consistent
631 with the observational result of more sea-ice melt in the southern region.

632 Sea-ice melt happens first in the northern region and in the slope, and progresses
633 towards the south and coast. While this progression is observed in the CTRL simulation, LowCd
634 sea-ice melt peaks in December in every sub-region with the exception of the northern slope,
635 where melt peaks in November. The largest differences in sea-ice melt between CTRL and
636 LowCd are found at the coastal stations in January, where the largest differences in surface
637 temperature and salinity are also observed between these two simulations. The increased melt
638 in the LowCd simulation during the summer confirms the hypothesis that the lower surface
639 temperatures seen in the LowCd experiment (compared to CTRL) are due to recently melted
640 sea ice.

641 Maps of climatological summer (December to February), winter (June to August) and
642 annual meteoric, net sea-ice melt and total freshwater were also plotted for the CTRL
643 simulation (Figure 8). It provides a broader assessment of the freshwater distribution
644 throughout the WAP region. The observed onshore-offshore gradient in meteoric water is
645 present in the summer and also seen in the annual values. The summer sea-ice melt values are
646 larger towards the coast and southern region, in agreement with the observations. These high-
647 melt areas are also areas of high sea-ice formation during the winter. The annual net sea-ice
648 melt values, then, suggest net sea-ice formation near the coast and in Marguerite Bay, while
649 higher net sea-ice melt is seen in the northern shelf. Since the freezing signal is dampened in
650 the in-situ data due to vertical mixing, it is possible that the overall influence of sea ice melt is
651 overestimated towards the south given data is collected during the months of highest sea-ice
652 melt in that region.

653
654



655
 656 Figure 8: Annual climatology of fluxes (top row) of total freshwater (left column), meteoric freshwater (middle column) and sea
 657 ice melt (right column); summer (December-February) climatology of fluxes (middle row); and winter (June-August) climatology
 658 of fluxes (bottom row). Dashed lines represent 750-m isobath, taken to be the edge of the continental shelf, and the different
 659 symbols represent coastal (black dots), shelf (green) and slope (black diamonds) stations.
 660

661 5 Discussion and Conclusion

662 Different ocean-sea ice hindcast simulations were conducted for a region encompassing
 663 the West Antarctic Peninsula (WAP) with different choices of wind-sea ice drag coefficient and
 664 parameterizations for Langmuir circulation to assess the effects of wind mixing and sea ice in
 665 the seasonal and interannual representation of MLD and freshwater cycles. Two different
 666 approaches to parameterizing Langmuir circulation were tested, based on the studies of Li et al.
 667 (2017) and Li and Fox-Kemper (2017). These approaches were applied to the KPP mixing
 668 parameterization and, respectively, include a Langmuir circulation-based enhancement term for
 669 wind mixing throughout the ocean surface mixed layer (Li et al., 2017) and a change in the
 670 vertical velocity scale in the critical Richardson number to increase entrainment of subsurface
 671 water from below the mixed layer (Li and Fox-Kemper, 2017).

672 We found that while the choice of LC parameterization does not significantly change
 673 simulated sea ice, the choice of wind-sea-ice drag coefficient lead to large differences in the
 674 representation of seasonal and interannual sea-ice variability. Since models are built to
 675 represent realistic physics, the model sensitivity to different parameterizations helps to

676 understand the influence of the processes parameterized in the real ocean. Therefore, this
677 study implies that while wind action has a large impact on sea-ice cycle, the role of LC in driving
678 sea-ice variability is limited. The CTRL simulation, which has a higher drag coefficient (2×10^{-3}),
679 shows a bias towards higher SIC and late sea-ice retreat when compared to the observations.
680 These biases are amplified in the simulation with low (5×10^{-4}) drag coefficient. The difference
681 between simulations with different drag coefficients is much larger during the period of sea-ice
682 retreat than during sea-ice advance, suggesting retreat is more influenced by wind action. The
683 small differences in SIC during sea-ice advance can potentially be explained by thermodynamic
684 effects. The sea-ice freezing temperature is higher for low-salinity waters, and earlier sea-ice
685 advance is seen in simulations with lower surface temperature and salinity.

686 Both sea ice and LC impact the MLD in the WAP. The influence of sea ice on surface MLD
687 is larger in the coastal and shelf regions, while the importance of LC for the MLD is larger than
688 that of sea ice close to the sea ice margins (slope) during the winter. Shallower spring and
689 summer MLD in the experiment with low drag coefficient (compared to CTRL) leads to
690 shallower MLD in the fall and winter despite this experiment having similar physics to the CTRL
691 simulation in the ice-free months, suggesting a lasting effect of improperly simulating summer
692 sea ice.

693 A bias towards MLD being shallower than that observed has been seen in several
694 modeling studies. For the LC parameterization, the mixed-layer entrainment approach
695 proposed by Li and Fox-Kemper (2017) proved to be more effective in deepening the MLD than
696 using an enhancement factor for wind mixing. Although the CTRL simulation includes the
697 parameterization of Li and Fox-Kemper (2017) and a higher wind-sea-ice drag coefficient, the
698 CTRL simulation still shows a bias towards shallow MLD compared to observations despite
699 being the best performing simulation and being able to better capture interannual variability.
700 While the interannual variability of MLD was reasonably simulated in most of the domain, the
701 model failed to properly capture it in the northern coast and southern slope sub-regions. The
702 northern coast is presumably highly influenced by sub-grid-scale phenomena that are not fully
703 reproduced by the model, and which can potentially explain the poor model performance
704 there; it is unclear at the moment why the model fails to capture MLD variability in the
705 southern slope.

706 Interannual variability of the freshwater cycle in the region cannot be studied from the
707 model results given that glacial inputs are based on estimated climatological values. However,
708 because the model reasonably represents sea ice and is thought to have realistic values for
709 meteoric sources, it is possible to do an assessment of the climatological importance of the
710 different freshwater sources in the region in different seasons. Overall, the model is able to
711 reproduce the basic patterns encountered in the observations, such as an onshore-offshore
712 gradient in meteoric freshwater and more sea-ice melt in the coastal and southern region
713 (compared to the northern part of the domain) in late summer. The regions of high sea-ice

714 melt in late summer are also regions of high sea-ice formation during the winter, and annual
715 sea-ice melt values indicate net sea ice formation near the coast and in Marguerite Bay, with
716 highest overall net sea-ice melt happening in the northern shelf of the domain.

717 Some of the changes to the model that could potentially improve the results further rely
718 on phenomena for which there is very little data, such as circulation in the coastal ocean and
719 Marguerite Bay, interannual variability of glacial freshwater discharges and sea-ice volume
720 (thickness). Although the largest sea-ice thicknesses simulated by the model are of the order of
721 one meter, which is in accordance with the scarce observations, data describing spatial and
722 temporal changes in sea-ice volume are not available. More measurements on these properties
723 would help quantify the freshwater cycle and its influence on surface water stratification. Since
724 most data in the Southern Ocean are collected in areas of open ocean and during the summer,
725 it is possible that there are biases in the initial conditions of ocean temperature and salinity
726 used for the model.

727 Despite the biases in the model results, this study highlights the influence of sea-ice
728 dynamics in the surface ocean mixing and freshwater fluxes, and the importance of proper
729 choice of parameters when simulating sea ice. Although the model results suggest that using
730 drag coefficients on the higher end of observed values leads to better results in this region of
731 the WAP, it is important to consider that reanalysis products underestimate wind speed and
732 therefore might be inducing the choice of higher drag coefficients to compensate for the model
733 bias. The study also stresses the potential of Langmuir circulation in deepening the MLD in the
734 Southern Ocean, and agrees with previous studies that the lack of properly parameterizing this
735 phenomenon could be partially responsible for the shallow MLD seen in model results.

736

737 **Acknowledgements**

738 The authors thank the many scientists, students, technicians, and ship captains, officers and
739 crew involved in the collection of the Palmer LTER historical time-series data. C. Schultz and S.
740 Doney acknowledge support by the US National Science Foundation (grant PLR-1440435 to the
741 Palmer Long Term Ecological Research program) and support from the University of Virginia. W.
742 G. Zhang acknowledge support by the US National Science Foundation (grant OPP-1643901).
743 The MITgcm model is an open source model (mitgcm.org). The version used in this study, with
744 added parameterizations and specific configurations, are on C. Schultz's github
745 (https://github.com/crisoceano/WAP_MITgcm). A copy of the files with specific configurations
746 for this study, the forcing files needed for the simulations, and a copy of the files used for the
747 KPP package are in three separate records on zenodo.org, under DOIs
748 10.5281/zenodo.3627365, 10.5281/zenodo.3627564, and 10.5281/zenodo.3627742.

749

750

751

752 **References**

753

754 Andreas, E.L., Tucker, W.B. III & Ackley, S.F. (1984), Atmospheric boundary-layer modification,
755 drag coefficient, and surface heat flux in the Antarctic marginal ice zone. *Journal of Geophysical*
756 *Research*, 89 (C1): 649-661. doi:10.1029/JC089iC01p00649

757

758 Andreas, E.L., Horst, T.W., Grachev, A.A., Persson, P.O., Fairall, C.W., Guet, P.S. & Jordan, R.E.
759 (2010), Parametrizing turbulent exchange over summer sea ice and the marginal ice zone.
760 *Quarterly Journal of the Royal Meteorological Society*, 136, 927-943. doi:10.1002/qj.618

761

762 Annett, A.L., Fitzsimmons, J.N., Séguret, M.J.M., Lagerström, M., Meredith, M.P., Schofield, O. &
763 Sherrell, R.M. (2017), Controls on dissolved and particulate iron distributions in surface waters
764 of the Western Antarctic Peninsula shelf. *Marine Chemistry*, 196, 81-97.
765 doi:10.1016/j.marchem.2017.06.004.

766

767 Belcher, S.E., Grant, A.L.M., Hanley, K.E., Fox-Kemper, B., Van Roekel, L., Sullivan, P.P., Large,
768 W.G., Brown, A., Hines, A., Calvert, D., Rutgersson, A., Pettersson, H., Bidlot, J., Janssen,
769 P.A.E.M. & Polton, J.A. (2012), A global perspective on Langmuir turbulence in the ocean
770 surface boundary layer. *Geophysical Research Letters*, 39, L18605, 2012.
771 doi:10.1029/2012GL052932

772 Birnbaum, G. & Lüpkes, C. (2002), A new parameterization of surface drag in the marginal ice
773 zone. *Tellus A: Dynamic meteorology and Oceanography*, 54A: 107-123.
774 doi:10.3402/tellusa.v54i1.12121

775 Boyer, T. P., Antonov, J. I., Baranova, O. K., Garcia, H. E., Johnson, D. R., Locarnini, R. A.,
776 Mishonov, A. V., O'Brien, T. D., Seidov, D., Smolyar, I. V. & Zweng, M. M. (2009), *World Ocean*
777 *Database 2009, Chapter 1: Introduction*, in S. Levitus (ed.), NOAA Atlas NESDIS 66, World Ocean
778 Database 2009, U.S. Gov. Printing Office, Wash. D.C., p. 216.

779

780 Bracegirdle, T.J., & Marshall, G.J. (2012), The reliability of Antarctic Tropospheric Pressure and
781 Temperature in the latest Global Reanalyses. *Journal of Climate*, 25, 7138-7146.
782 doi:10.1175/JCLI-D-11-00685.1

783

784 Castellani, G., Lüpkes, C., Hendricks, S. & Gerdes, R. (2014), Variability of sea-ice topography
785 and its impact on the atmospheric surface drag. *Journal of Geophysical Research Oceans*, 119,
786 6743-6762. doi:10.1002/2013JC009712

787

788 Comiso, J. C. (2017). Bootstrap Sea Ice Concentrations from Nimbus-7 SMMR and DMSP SSM/I-
789 SSMIS, Version 3. Boulder, Colorado USA. NASA National Snow and Ice Data Center Distributed
790 Active Archive Center. doi: 10.5067/7Q8HCCWS4I0R

791

792 Cook, A.J., Fox, A.J., Vaughan, D.G. & Ferrigno, J.G. (2005), Retreating glacier fronts on the
793 Antarctic Peninsula over the past half-century. *Science*, 308, 541-544.
794 doi:10.1126/science.1104235
795

796 D'Asaro, E.A. (2014), Turbulence in the upper-ocean mixed layer, *Annual Reviews in Marine*
797 *Sciences*, 6, 101-115. doi:10.1146/annurev-marine-010213-135138
798

799 Dee, D. P., Uppala, S. M., Simmons, A. J., Berrisford, P., Poli, P., Kobayashi, S., Andrae, U.,
800 Balmaseda, M. A., Balsamo, G., Bauer, P., Bechtold, P., Beljaars, A. C. M., van de Berg, L., Bidlot,
801 J., Bormann, N., Delsol, C., Dragani, R., Fuentes, M., Geer, A. J., Haimberger, L., Healy, S. B.,
802 Hersbach, H., Holm, E. V., Isaksen, L., Kallberg, P., Kohler, M., Matricardi, M., McNally, A. P.,
803 Monge-Sanz, B. M., Morcrette, J.-J., Park, B.-K., Peubey, C., de Rosnay, P., Tavolato, C., Thepaut,
804 J.-N. & Vitart, F. (2011), The ERA-Interim reanalysis: configuration and performance of the data
805 assimilation system, *Quarterly Journal of the Royal Meteorological Society*, 137(656): 553–597.
806 doi:10.1002/qj.828
807

808 Doble, M. J., M. D. Coon & P. Wadhams (2003), Pancake ice formation in the Weddell Sea.
809 *Journal of Geophysical Research: Oceans*, 108(C7). doi:10.1029/2002JC001373
810

811 Ducklow, H.W., Fraser, W.R., Meredith, M.P., Stammerjohn, S.E., Doney, S.C, Martinson, D.G.,
812 Sailley, S.F., Schofield, O.M., Steinberg, S.K., Venables, H.J. & Amsler, C.D. (2013), West
813 Antarctic Peninsula: An ice-dependent coastal marine ecosystem in transition. *Oceanography*,
814 26(3), 190-203.
815

816 Fretwell, P., Pritchard, H.D., Vaughan, D.G., Bamber, J.L., Barrand, N.E., Bell, R., Bianchi, C.,
817 Bingham, R.G., Blankenship, D.D., Casassa, G., Catania, G., Callens, D., Conway, H., Cook, A.J.,
818 Corr, H.F.J., Damaske, D., Damm, V., Ferraccioli, F., Forsberg, R., Fujita, S., Gim, Y., Gogineni, P.,
819 Griggs, J.A., Hindmarsh, R.C.A., Holmlund, P., Holt, J.W., Jacobel, R.W., Jenkins, A., Jokat, W.,
820 Jordan, T., King, E.C., Kohler, J., Krabill, W., Riger-Kusk, M., Langley, K.A., Leitchenkov, G.,
821 Leuschen, C., Luyendyk, B.P., Matsuoka, K., Mouginot, J., Nitsche, F.O., Nogi, Y., Nost, O.A.,
822 Popov, S.V., Rignot, E., Rippin, D.M., Rivera, A., Roberts, J., Ross, N., Siegert, M.J., Smith, A.M.,
823 Steinhage, D., Studinger, M., Sun, B., Tinto, B.K., Welch, B.C., Wilson, D., Young, D.A., Xiangbin,
824 C. & Zirizzotti, A. (2013), Bedmap2: improved ice bed, surface and thickness datasets for
825 Antarctica Cryosphere 7, 375–393. doi:10.5194/tc-7-375-2013
826

827 Grant, A. L. M. & S. E. Belcher (2009), Characteristics of Langmuir turbulence in the ocean mixed
828 layer. *Journal of Physical Oceanography*, 39, 1871–1887. doi:10.1175/2009JPO4119.1
829

830 Hauck, J., Völker, C., Wolf-Gladrow, D.A., Laufkötter, C., Vogt, M., Aumont, O., Bopp, L.,
831 Buitenhuis, E.T., Doney, S.C., Dunne, J., Gruber, N., Hashioka, T., John, J., Le Quéré, C., Lima,
832 I.D., Nakano, H., Sérfian & R., Totterdell, I. (2015), On the Southern Ocean CO₂ uptake and the
833 role of the biological carbon pump in the 21st century. *Global Biogeochemical Cycles*, 29, 1451-
834 1470. doi:10.1002/2015GB005140
835

836 Holland, P.R., Bruneau, N., Enright, C., Losch, M., Kurtz, N.T. & Kwok, R. (2014), Modeled Trends
837 in Antarctic Sea Ice thickness. *Journal of Climate*, 27, 3784-3801. doi:10.1175/JCLI-D-13-00301.1
838

839 Kim, H., Doney, S.C., Iannuzzi, R.A., Meredith, M.P., Martinson, D.G. & Ducklow, H.W. (2016),
840 Climate forcing for dynamics of dissolved inorganic nutrients at Palmer Station, Antarctica: An
841 interdecadal (1993–2013) analysis. *Journal of Geophysical Research: Biogeosciences*, 121 (9),
842 2369–2389. doi:10.1002/2015JG003311
843

844 Klinck, J.M., Hofmann, E.E., Beardsley, R.C., Salihoglu, B. & Howard, S. (2004), Watermass
845 properties and circulation on the west Antarctic Peninsula continental shelf in austral fall and
846 winter 2001. *Deep Sea Research Part II: Topical Studies in Oceanography*, V 51, issues 17-19,
847 1925-1946. doi:10.1016/j.dsr2.2004.08.001
848

849 Kohout, A. L., Williams, M. J. M., Dean, S. M., & Meylan, M. H. (2014), Storm-induced sea-ice
850 breakup and the implications for ice extent. *Nature*, 509, 604. doi:10.1038/nature13262
851

852 Large, W.G., McWilliams, J.C. & Doney, S.C. (1994), Oceanic vertical mixing: A review and a
853 model with a nonlocal boundary layer parameterization. *Reviews of Geophysics*, 32, 363-403.
854 doi: 10.1029/94RG01872
855

856 Legge, O.J., Bakker, D.C.E., Meredith, M.P., Venables, H.J., Brown, P.J., Jones, E.M. & Johnson,
857 M.T. (2017), The seasonal cycle of carbonate system processes in Ryder Bay, West Antarctic
858 Peninsula. *Deep Sea Research Part II: Topical Studies in Oceanography*, v. 139, 167-180. doi:
859 10.1016/j.dsr2.2016.11.006
860

861 Li, S., Li, M., Gerbi, G. P. & Song, J. (2013), Roles of breaking waves and Langmuir circulation in
862 the surface boundary layer of a coastal ocean. *Journal of Geophysical Research Oceans*, 118
863 (10): 5173-5187. doi: 10.1002/jgrc.20387
864

865 Li, Q., Fox-Kemper, B., Breivik, O & Webb, A. (2017), Statistical models of global Langmuir
866 mixing. *Ocean Modelling*, 113, 95-114. doi: 10.1016/j.ocemod.2017.03.016
867

868 Li, Q., & Fox-Kemper, B. (2017), Assessing the Effects of Langmuir Turbulence on the
869 Entrainment Buoyancy Flux in the Ocean Surface Boundary layer. *Journal of Physical
870 Oceanography*, v 47, 2863-2886. doi: 10.1175/JPO-D-17-0085.1
871

872 Losch, M. (2008), Modeling ice shelf cavities in a z coordinate ocean general circulation model.
873 *Journal of Geophysical Research*, 113(C8), C08043. doi: 10.1029/2007JC004368
874

875 Losch, M., Menemenlis, D., Campin, J.M., Heimbach, P. & Hill, C. (2010), On the formulation of
876 sea-ice models. Part 1: Effects of different solver implementations and parameterizations.
877 *Ocean Modelling*, 33, 129-144. doi: 10.1016/j.ocemod.2009.12.008
878

879 Marshall, J., Adcroft, A., Hill, C., Perelman, L. & Heisey, C. (1997), A finite-volume,
880 incompressible Navier-Stokes model for studies of the ocean on parallel computers. *Journal of*
881 *Geophysical Research*, 102, 5753-5766. doi: 10.1029/96JC02775
882
883 Marshall, J., Hill, C., Perelman, L. & Adcroft, A. (1997), Hydrostatic, quasi-hydrostatic, and
884 nonhydrostatic ocean modeling. *Journal of Geophysical Research*, 102(C3):5733-5752. doi:
885 10.1029/96JC02776
886
887 Martinson, D.G., Stammerjohn, S.E., Ianuzzi, R.A., Smith, R.C. & Vernet, M. (2008), Western
888 Antarctic Peninsula physical oceanography and spatio-temporal variability. *Deep-Sea Research*
889 *II*, 55, 1964-1987. doi: 10.1016/j.dsr2.2008.04.038
890
891 McWilliams, J.C. & Sullivan, P.P. (2000), Vertical mixing by Langmuir circulations. *Spill Science &*
892 *Technology Bulletin*, v 6, issues 3-4, 225-237. Doi: 10.1016/S1353-2561(01)00041-X
893
894 McWilliams, J.C., Huncke, E., Liang, J. & Sullivan, P.P. (2014), Langmuir turbulence in swell.
895 *Journal of Physical Oceanography*, 44, 870-890. doi: 10.1175/JPO-D-13-0122.1
896
897 Meredith, M.P. & King, J.C. (2005), Rapid climate change in the ocean west of the Antarctic
898 Peninsula during the second half of the 20th century. *Geophysical Research Letters*, 32, 1-5. doi:
899 10.1029/2005GL024042
900
901 Meredith, M.P., Brandon, M.A., Wallace, M.I., Clarke, A., Leng, M.J., Renfrew, I.A., van Lipzig,
902 N.P.M. & King, J.C. (2008), Variability in the freshwater balance of northern Marguerite Bay,
903 Antarctic Peninsula: results from $\Delta^{18}\text{O}$, *Deep Sea Research Part II: Topical Studies in*
904 *Oceanography*, 55, 309–322. doi: 10.1016/j.dsr2.2007.11.005
905
906 Meredith, M.P., Venables, H.J., Clarke, A., Ducklow, H.W., Erickson, M., Leng, M.J., Lenaerts,
907 J.T.M. & Van den Broeke, M.R. (2013), The Freshwater System West of the Antarctic Peninsula:
908 Spatial and Temporal Changes. *Journal of Climate*, 26, 1669-1684. doi: 10.1175/JCLI-D-12-
909 00246.1
910
911 Meredith, M.P., Stammerjohn, S.E., Venables, H.J., Ducklow, H.W., Martinson, D.G., Ianuzzi,
912 R.A., Leng, M.J., van Wesseem, J.M., Reijmer, C.H. & Barrand, N.E. (2017), Changing distributions
913 of sea ice melt and meteoric water west of the Antarctic Peninsula. *Deep Sea Research Part II:*
914 *Topical Studies in Oceanography*. V. 129, 40-57. doi: 10.1016/j.dsr2.2016.04.019
915
916 Miller, P.A., Laxon, S.W., Feltham, D.L. & Cresswell, D.J. (2006), Optimization of sea ice model;
917 using basinwide observations of Arctic sea ice thickness, extent and velocity. *Journal of Climate*,
918 19, 1089-1108. doi: 10.1175/JCLI3648.1
919
920 Mitchell, B.G. & Holm-Hansen, O. (1991), Observations of modeling of the Antarctic
921 phytoplankton crop in relation to mixing depth. *Deep Sea Research Part A. Oceanographic*
922 *Research Papers*, v 38, issues 8-9, 981-1007.

923
924 Moffat, C., Beardsley, R.C., Owens, B. & van Lipzig, N. (2008), A first description of the Antarctic
925 Peninsula Coastal Current. *Deep-Sea Research Part II, Topical Studies in Oceanography*, 55, 277-
926 293. doi: 10.1016/j.dsr2.2007.10.003
927
928 Moffat, C. & Meredith, M. (2018), Shelf–ocean exchange and hydrography west of the Antarctic
929 Peninsula: a review. *Philosophical Transactions of the Royal Society A*, 376: 20170164. doi:
930 10.1098/rsta.2017.0164

931 Noh, Y. & Lee, W.S. (2008), Prediction of the mixed and mixing layer depths from an OGCM.
932 *Journal of Oceanography*, 64, 217-225. doi:10.1007/s10872-008-0017-1.

933 Phillips, O.M. (1985), Spectral and statistical properties of the equilibrium range in wind-
934 generated gravity waves. *Journal of Fluid Mechanics*, 156, 505-531.
935 doi:10.1017/S0022112085002221

936 Regan, H.C., Holland, P.R., Meredith, M.P. & Pike, J. (2018), Sources, variability and fate of
937 freshwater in the Bellingshausen Sea, Antarctica. *Deep-Sea Research Part I: Oceanographic*
938 *Research Papers*, 133, 59-71. doi: 10.1016/j.dsr.2018.01.005
939
940 Schiller, A. & Ridgway., K.R. (2013), Seasonal mixed-layer dynamics in an eddy-resolving ocean
941 circulation model. *Journal of Geophysical Research Oceans*, 118, 3387-3405.
942 Doi:10.1002/jgrc.20250
943
944 Smith, M., Stammerjohn, S., Persson, O., Rainville, L., Liu, G. & Perrie, W. (2018), Episodic
945 reversal of autumn ice advance caused by release of ocean heat in the Beaufort Sea. *Journal of*
946 *Geophysical Research: Oceans*, 123, 3164–3185. doi:10.1002/2018JC013764
947
948 Stammerjohn, S.E., Martinson, D.G., Smith, R.C. & Ianuzzi, R.A. (2008), Sea ice in the western
949 Antarctic Peninsula region: Spatio-temporal variability from ecological and climate change
950 perspectives. *Deep-Sea Research Part II*, 55, 2041-2058. doi: 10.1016/j.dsr2.2008.04.026
951
952 Stammerjohn, S., Massom, R. A., Rind, D., & Martinson, D. (2012), Regions of rapid sea ice
953 change: An inter-hemispheric seasonal comparison. *Geophysical Research Letters*, 39 (L06501).
954 doi: 10.1029/2012GL050874
955
956 Talley, L.D., Pickard, G.L., Emery, W.J. & Swift, J.H. (2011), *Descriptive Physical Oceanography: An*
957 *Introduction* (sixth edition), Elsevier, Boston, 560 pp.
958
959 Taylor, M.H., Losch, M. & Bracher, A. (2013), On the drivers of phytoplankton blooms in the
960 Antarctic marginal ice zone: a modeling approach. *Journal of Geophysical Research: Oceans*,
961 118, 63-75. doi: 10.1029/2012JC008418
962

963 Tsamados, M., Feltham, D.L., Schroeder, D. & Flocco, D. (2014), Impact of variable atmospheric
964 and oceanic form drag on simulations of Arctic sea ice. *Journal of Physical Oceanography*, 44(5),
965 1329-1353. doi: 10.1175/JPO-D-13-0215.1
966

967 Turner, J., Lu, H., White, I., King, J.C., Phillips, T., Hosking, J.S., Bracegirdle, T.J., Marshall, G.J.,
968 Mulvaney, R. & Deb, P. (2016), Absence of 21st century warming on Antarctic Peninsula
969 consistent with natural variability. *Nature*, 535, 411–415. doi: 10.1038/nature18645
970

971 Van Wessem, J.M., Meredith, M.P., Reijmer, C.H., van den Broeke, M.R. & Cook, A.J. (2016),
972 Characteristics of the modelled meteoric freshwater budget of the western Antarctic Peninsula,
973 *Deep Sea Research Part II: Topical Studies in Oceanography*, 139, 31-39.
974 doi:10.1016/j.dsr2.2016.11.001
975

976 Vaughan, D.G., Marshall, G.J., Connolley, W.M., Parkinson, C., Mulvaney, R., Hodgson, D.A.,
977 King, J.C., Pudsey, C.J. & Turner, J. (2003), Recent Rapid Regional Climate Warming on the
978 Antarctic Peninsula. *Climatic Change*, 60, 243-274, 2003. doi: 10.1023/A:1026021217991
979

980 Vernet, M., Martinson, D., Ianuzzi, R., Stammerjohn, S., Kozlowski, W., Sines, K., Smith, R. &
981 Garibotti, I. (2008), Primary production within the sea-ice zone west of the Antarctic Peninsula:
982 I – Sea ice, summer mixed layer, and irradiance. *Deep-Sea Research Part II*, 55, 2068-2085. doi:
983 10.1016/j.dsr2.2008.05.021
984

985 Wamser, C. & Martinson, D.G. (1993), Drag Coefficients for Winter Antarctic Pack Ice. *Journal of*
986 *Geophysical Research: Oceans*, v. 98 (C7), 12,431-12,437. doi:10.1029/93JC00655
987

988 Webb, A., & Fox-Kemper, B. (2015), Impacts of wave spreading and multidirectional waves on
989 estimating stokes drift. *Ocean Modelling*, 96, 49-64. doi: 10.1016/j.ocemod.2014.12.007
990
991
992
993
994
995
996
997
998